Nanoscale

Accepted Manuscript

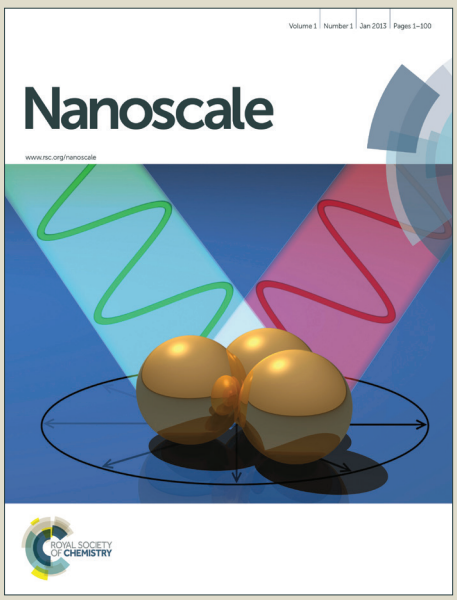

ROYAL SOCIETY OF CHEMISTRY

www.rsc.org/nanoscale

Cite this: DOI: 10.1039/c0xx00000x

www.rsc.org/xxxxxx

ARTICLE TYPE

Sulfur-doped porous reduced graphene oxide hollow nanospheres framework as metal-free electrocatalysts for oxygen reduction reaction and supercapacitor electrode materials

Xi'an Chen,[a,b] Xiaohua Chen,*[a] Xin Xu,[b] Zhi Yang,[b] Zheng Liu,[a] Lijie Zhang,[b] Xiangju Xu,[b] Ying Chen[c] and Shaoming Huang*[b]

Received (in XXX, XXX) Xth XXXXXXXXX 20XX, Accepted Xth XXXXXXXXX 20XX
DOI: 10.1039/b000000x

Chemical doping with foreign atoms is an effective approach to significantly enhance electrochemical performance of the carbon materials. Herein, sulfur-doped three-dimensional (3D) porous reduced graphene oxide (RGO) hollow nanospheres framework (S-PGHS) is fabricated by directly annealing graphene oxide (GO)-encapsulated amino-modified SiO_2 nanoparticles with dibenzyl disulfide (DBDS), and followed by hydrofluoric acid etching. The XPS and Raman spectra confirm that sulfur atoms have been successfully introduced into PGHS framework via covalent bonds. The as-prepared S-PGHS has been demonstrated to be an efficient metal-free electrocatalyst for oxygen reduction reaction (ORR) with the activity comparable with that of commercial Pt/C (40%), and much better methanol tolerance and durability, and to be supercapacitor electrode material with a high specific capacitance of 343 F g^{-1}, good rate capability and excellent cycling stability in aqueous electrolytes. The impressive performance for ORR and supercapacitor is believed to be due to the synergistic effect caused by sulfur-doping enhancing the electrochemical activity and 3D porous hollow nanospheres framework structure facilitating ion diffusion and electronic transfer.

Introduction

The oxygen reduction reaction (ORR) is one of the most important processes in energy conversion systems such as fuel cells[1] and metal-air batteries,[2] as well as in other applications including water purification, oxygen detection, and corrosion protection[3,4]. Platinum-based materials are known to be the most active cathode catalysts for ORRs.[5-7] However, the high cost, limited supply and weak durability of platinum catalysts in the fuel-cell environment have greatly impeded the commercialization of fuel cells and limited their performance.[1, 5] Therefore, the ongoing search for new non-precious-metal catalysts (NPMCs) with excellent electrocatalytic performance for ORRs has aroused great interest. Carbonaceous materials including heteroatom-doped carbons, graphitic-C_3N_4-based and graphene-based materials have been explored for ORR owing to their low cost, environmental friendliness, high activity and long durability [8-14]. Among those carbon-based materials, graphene, the distinct two dimensional sp^2-hybridized carbon networks, possesses remarkable conductivity and excellent mechanical properties, which endow it as ideal alternative catalyst for ORR more than its role as a conductive support [15-21]. Previously, we have reported S-doped graphene as metal-free cathode catalyst for ORR exhibit good performance with high activities and long lifetimes.[22] However, graphene-based materials usually suffer from their serious agglomeration during fabrication, which causes inferior ionic accessibility and thus modest improvement in the cell performance. Recent reports and reviews have revealed that electrode construction consisting of three-dimensional (3D) interpenetrating structures can significantly enhance electron transfer and facilitate faster reactants' mass transfer, thereby resulting in high-performance devices, such as supercapacitor, lithium ion batteries, and fuel cells [23-25]. Our recent efforts have also discovered that 3D conductive network carbon materials can improve the performance for supercapacitor and ORR [26-28].

As energy storage devices, supercapacitors have also received extensive attention due to their unique advantages including long cycle life, excellent reversibility, and high energy and power density.[29, 30] Carbonaceous materials including activated carbon (AC), mesoporous carbon (MC), carbon nanotubes, and graphene *etc*. are the type of good candidates for electrochemical double-layer capacitors (EDLCs).[15, 31, 32] Among these, graphene with high electronic conductivity and large specific surface area (SSA) has been widely explored as electrode materials with specific capacitance of 100-260 F g^{-1} in KOH aqueous solution.[33-37] Building of 3D structure graphene through the introduction fillers or dopants, such as conducting polymers, other nanostructured carbon and heteroatoms,[38-42] can also improve the capacitance of graphene-based ECs. To our knowledge, sulfur-doped 3D structure carbon nanomaterials have rarely been investigated for supercapacitors.

In this text, sulfur-doped 3D porous RGO hollow nanospheres framework (S-PGHS) was produced by directly annealing GO-

encapsulated amino-modified SiO_2 nanoparticles with DBDS, and followed by hydrofluoric acid etching. S-PGHS used as metal-free ORR electrocatalysts exhibits excellent activity with four electron transfer, and much better methanol tolerance and durability than commercial Pt/C (40 wt.%) in alkaline media. Meanwhile, S-PGHS was evaluated for supercapacitor electrode material, displaying high specific capacitance, good rate capability and excellent cycling stability. The remarkable electrochemical performance makes it an attractive electrode material for various energy storage devices.

Experimental

Materials synthesis

SiO_2 nanoparticles (1 g) with the size of about 200 nm were dispersed into dry toluene (300 mL) by a sonication process to form a suspension. 3-Aminopropyltrimethoxysilane (3 mL) was added to the suspension under stirring, and heated at a temperature of 65 ^oC for 12 h. Amino-modified SiO_2 nanoparticles (SiO_2-NH_2) were produced after centrifugation at 10000 rpm for 5 min followed by dry process under vacuum at 60 ^oC for 3 h. The SiO_2-NH_2 nanoparticles (1g) were re-dispersed in water with ultrasound for 10 min to generate a suspension. 1 mg mL^{-1} GO solution (200 ml) prepared from graphite flakes by the modified Hummers Method[26] were added to the suspension and heated at a temperature of 65 ^oC for 10 h under stirring. After centrifugation at 10000 rpm for 5 min, SiO_2@GO composites were re-dispersed in alcohol containing DBDS (0.6 g) with ultrasound for 5 min. The resulting suspension was dried, forming a uniform solid mixture. The mixtures were placed into a quartz tube with Ar atmosphere and annealed at 900 ^oC for 30 min with a heating rate of 10 ^oC min^{-1}. After cooled to room temperature, SiO_2@ S-doped GO (SiO_2@S-G) was collected from the quartz tube. Then, 3D S-doped porous RGO hollow nanospheres (S-PGHS) framework (0.12 g) was generated by further treatment of SiO_2@S-G composite with 10% HF for 6h followed by washed with ultrapure water and vacuum dry with a yield of about 60%. As a control experiment, other carbon materials obtained under various conditions such as the annealing temperature including 1000, 900, 750, 600 ^oC (the mass ratios of DBDS to GO is 3:1) and the mass ratios of DBDS to GO with 1:1, 3:1, 5:1 (annealing temperature is 900) were synthesized in the same way. The resulted materials are denoted S-PGHS-1000, S-PGHS-900, S-PGHS-750, S-PGHS-600, S-PGHS-1-1, S-PGHS-5-1, and so on. Two dimension RGO without being dealt with SiO_2 (S-2DG-900) and PGHS without any dopants (PGHS-900) were treated under the same condition.

Electrode preparation and Electrochemical measurements

Glassy carbon (GC) or rotating-disk GC electrodes (3 mm diameter, CH instrument Inc.) were polished with a 0.3 and 0.05 mm alumina slurry (CH Instrument Inc.) successively and rinsed with ultrapure water and ethanol. The electrodes were then sonicated in ultrapure water, rinsed thoroughly with ultrapure water and dried under a gentle nitrogen stream. To prepare the working electrode for ORR, all of carbon materials (2 mg) were ultrasonically dispersed in ethanol (4 mL) under the same process, 10 μL of the resulting suspension were dropped onto the GC surface and dried at room temperature for 4 h. Then Nafion (0.5%) solution 5 μL was dropped on GC with PGHS samples and dried at room temperature. For comparison, a commercially available Pt/C catalyst (40 wt% Pt) modified GC working electrode was prepared in the same way. As for the supercapacitor electrodes preparation, similar treatment was adopted other than this process that 40 μg carbon nanomaterials were dropped into GC electrode (4 mm diameter, CH instrument Inc.).

All electrochemical measurements on ORR, including cyclic voltammograms (CV), rotating-disk electrode Linear sweep voltammetry (LSV) and chronoamperometry, were performed at room temperature in 0.1 M KOH solutions by a three-electrode cell, in which platinum-wire was used as counter electrode and Ag//AgCl (in sat. KCl) as reference electrode, which were purged with high purity nitrogen or oxygen for at least 30 min prior to each measurement. All electrochemical measurements on capacitance performance carried out in a three-electrode cell, where platinum-wire was used as counter electrode and Ag//AgCl (in sat. KCl) as reference electrode with electrolyte of 2 M KOH aqueous solution under atmosphere.

The Koutecky-Levich plots were obtained by linear fitting of the reciprocal rotating speed versus reciprocal current density collected at different potentials form -0.4 V to -0.6 V. The overall electron transfer numbers per oxygen molecule involved in a typical ORR process can be calculated from the following two equations:

$$J^{-1}=J_k^{-1} + (B\,\omega^{1/2})^{-1} \qquad \textbf{equation 1}$$

$$B=0.62\,n\,F\,C_O\,D_O^{2/3}\,\nu^{-1/6} \qquad \textbf{equation 2}$$

where J_k is the kinetic current in amperes at a constant potential, ω is the electrode rotating speed in rpm, and B, the reciprocal of the slope, n is the number of electrons transferred per oxygen molecule, F is the Faraday constant（96485 C mol^{-1}）, C_O is the concentration of O_2 (1.2×10^{-3} mol L^{-1}), D_O is the diffusion coefficient of O_2 in 0.1 M KOH (1.9×10^{-5} cm s^{-1}) and ν is the kinetic viscosity of the electrolyte (ν=0.01 cm^2 s^{-1}).

The specific capacitance of the electrode was calculated from the CV curves according to **equation 3** [$C = \int I\,dV / (2\,m\,\upsilon\,\Delta V)$], where C is the specific capacitance (F/g), I is the oxidation or reduction current, m indicates the mass of active material(g), υ is the potential scan rate (mV/s), and ΔV indicates the voltage range of one sweep segment. Specific capacitance could also be calculated from the galvanostatic charge and discharge curves, using the **equation 4** [$C = I\,\Delta t / (m\,\Delta V)$], where I is charge or discharge current, Δt is the time for a full charge or discharge, m indicates the mass of active material, and ΔV represents the voltage change of a full charge or discharge.

Characterization

X-ray photoelectron spectroscopy (XPS) measurements were carried out with an ultrahigh vacuum setup, equipped with a monochromatic Al Ka X-ray source and a high resolution Thermo ESCALAB 250 analyzer. Raman spectra were collected on a Labram-010 microscopic confocal Raman spectrometer with a 633 nm laser excitation. Field emission scanning electron microscopy (FE-SEM) images and energy dispersive spectroscopy (EDS) were obtained with a Nova NanoSEM 200 scanning electron microscope (FEI, Inc.). Transmission electron microscopy (TEM), high-resolution transmission electron microscopy (HRTEM) images and STEM-EDS elemental mapping were recorded with a JEOL2100 instrument. The samples and KBr crystal were ground together, and pressed into a

flake for IR spectroscopy. Specific surface area and pore size distribution were determined on a Micromeritics ASAP 2020 instrument. Elemental analysis was conducted on the Vario EL elemental analyzer. ICP measurement was carried out using an inductively coupled plasma-mass spectrometry (Agilent 7700CE). All the electrochemical tests (CV, LSV, chronoamperometry, galvanostatic charge and discharge, Electrochemical Impedance Spectra) were recorded on a CHI660e electrochemical workstation (Shanghai Chenhua).

Results and discussion

The process of fabricating S-PGHS contains mainly three steps (Scheme 1): (i) SiO_2 spheres with the size of about 200 nm were modified by surface grafting of aminopropyltrimethoxysilane (APS); (ii) GO will be chemically bonded onto the SiO_2-NH_2 or adsorbed to the surface through electrostatic assembly to obtain the GO coated SiO_2 spheres (SiO_2@GO), then blending with a certain amount of DBDS; (iii) High temperature annealing process was conducted for doping the sulfur and removing oxygen containing groups and restoring graphene structure, and followed by dissolving the SiO_2 core with HF solutions to produce the S-PGHS, which used as metal-free electrocatalysts for ORR and supercapacitor electrode materials. From FT-IR (Fig. S1a), after reacted with aminopropyltrimethoxysilane, the peaks around 2970, 2930 cm^{-1} corresponding to -CH_3, -CH_2 stretching vibration were observed in SiO_2-NH_2. In addition, the two distorted peaks around 3300 cm^{-1} being assigned to -NH_2 stretching vibration appear in SiO_2-NH_2. These results indicate aminopropyltrimethoxysilane has been grafted onto the surface of silica spheres. The peak around 1730 cm^{-1} being assigned to C=O of COOH disappears in the FT-IR spectrum of GO@SiO_2 (Fig. S1b), indicating that the amidation reaction with COOH of GO and SiO_2-NH_2 has occurred.

The morphology and microstructure of the resulted SiO_2@GO and S-PGHS were observed by FESEM and TEM (Fig. 1). As can be seen from Fig. 1a, the GO sheets wrapping around the surface of individual or aggregated SiO_2 nanoparticles show crinkled and rough textures, which is related to the presence of flexible and ultrathin graphene sheets. The edges of individual and overlapping GO layers at the interface between aggregated particles can be observed, indicating the RGO layers appear to link neighboring spheres together. After annealing with sulfur precursor and followed a removal of the core SiO_2 nanospheres, sulfur doped porous RGO hollow nanospheres with thin and intact continuous walls are interconnected to 3D hierarchical frameworks (Fig. 1b, 1c). EDX profile (Fig. 1d) confirms the existence of elemental S in S-PGHS. From the image of TEM (Fig. 1e), S-doping RGO hollow nanospheres forming continuous frameworks can be easily observed, which is coincided with observation by SEM. The nitrogen sorption isotherm of S-PGHS-900 (Fig. S2a) displays a BET surface area of 496 m^2 g^{-1}. The pore size distribution curve (Fig. S2b) exhibits two peaks about at 2.7 nm and 17 nm. This hierarchical mesoporous structure facilitating the electrolyte ions migration into inlayers so that it is expected to improve the electrochemical performance of materials. From the STEM-EDS elemental mapping was performed (Fig. 1f-1i) and verified the homogeneous coating of sulfur throughout the 3D porous framework.

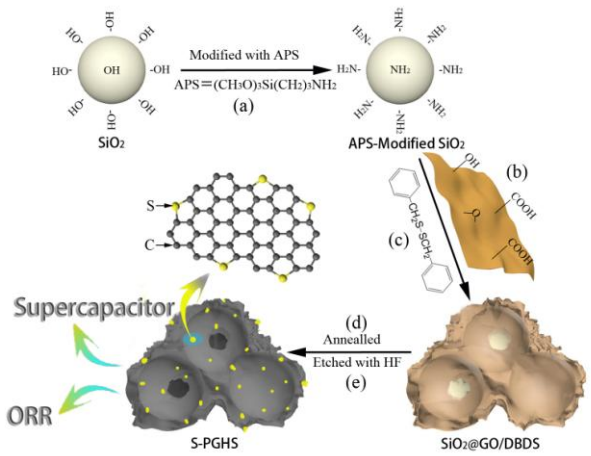

Scheme 1 Schematic illustration of S-PGHS preparation.

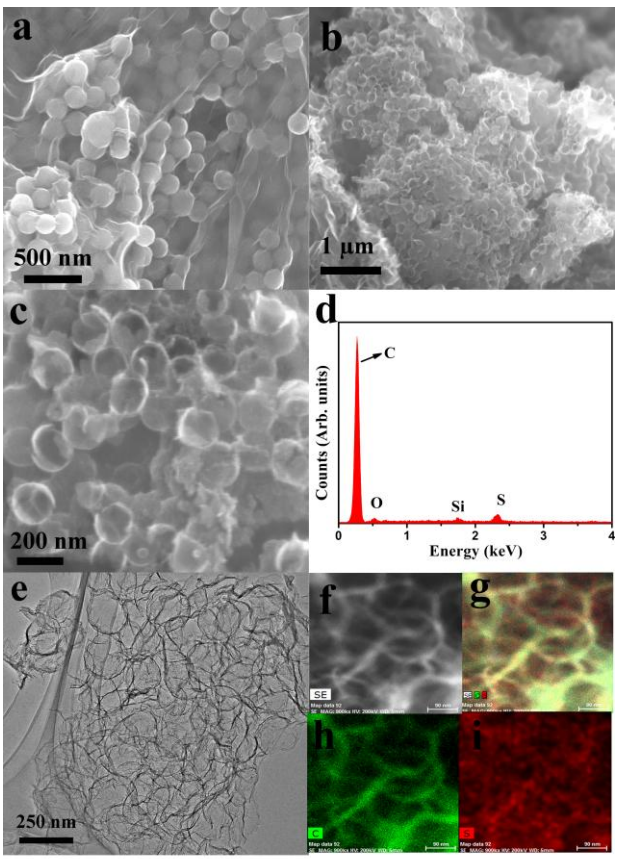

Fig. 1 SEM image of SiO_2@GO (a); SEM images at different magnification(b, c), TEM image (e) and STEM-EDS elemental mapping (f-i) of S-PGHS-900; EDX profile (d) of S-PGHS-900 in silicon slice.

The chemical compositions and status of sulfur element in these S-PGHS were further investigated using X-ray photoelectron spectroscopy (XPS) and Raman spectroscopy. The XPS spectrum of PGHS-900 (Fig. 2a) shows the presence of only carbon and oxygen atom. S-PGHS-900 show three visible peaks

corresponding to carbon (C 1s), oxygen (O 1s), sulfur (S 2p), respectively. As can be seen from the high-resolution S2p spectrum (Fig. 2b), S-PGHS-900 contains sulfur atoms which form C-S-C bond with neighboring carbon atoms like thiophene structures. Furthermore, SO_x groups being chemically inactive for ORR are not evident [22]. The N1s spectrum displays a no obvious peak around 400 eV indicating almost no amount of N is doped (Fig. S3), which is also verified by elemental analysis of S-PGHS-900 (Table S1). A possible reason is that the amount of NH_2 group on the surface is small, and NH_2 group with low thermal stability will lost during the annealing process. From Fig. S4, all the S-doped RGO samples show the presence of sulfur element and the S levels in S-PGHS-1000, S-PGHS-900, S-PGHS-750, S-PGHS-600, S-PGHS-900-1-1, S-PGHS-900-5-1, S-2DG-900, PGHS-900 are 1.19%, 1.99%, 1.01%, 0.78%, 1.23%, 1.14%, 1.1% and 0%, respectively (Table S2). S-PGHS-900 shows the highest levels of sulfur indicating S doping into PGHS framework at 900 ^oC is convenient. With increasing further the annealing temperature, the content of sulfur doped decreases, which may be due to sulfur doped escaping from the breaking of the minority C-S bonds. More amounts of DBDS used as sulfur source could only provide 1.19% sulfur doped may be due to the fact that there are plenty of residual carbons after the pyrolysis of DBDS. Moreover, Raman spectroscopy, as shown in Fig. 3 is another direct proof for the S doping of PGHS. After doped with sulfur atoms, the G peaks of the S-PGHS-900, S-PGHS-900-1-1, S-PGHS-900-5-1 samples down-shifted to 1582, 1581, 1582 cm^{-1}, respectively, compared to the peak at 1588 cm^{-1} of PGHS-900. This red shift is an important characteristic of n-type substitutional doping of graphene[43], and observed in S-graphenes our previously reported.[22] The XPS results and Raman spectroscopy verified that sulfur atoms have been successfully introduced into PGHS framework *via* covalent bonds.

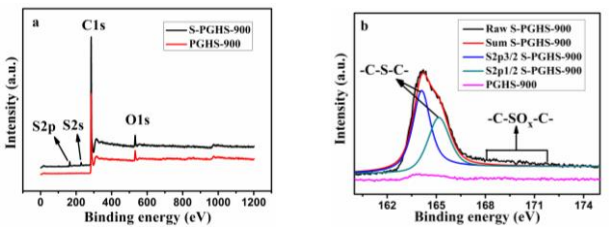

Fig. 2 XPS spectra of S-PGHS-900 and PGHS-900: (a) survey spectra, (b) S2p spectra.

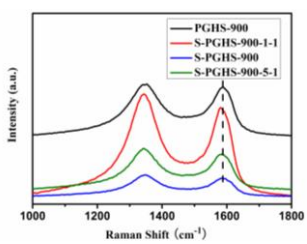

Fig. 3 Raman spectra of PGHS-900, S-PGHS-900-1-1, S-PGHS-900, S-PGHS-900-5-1.

The ORR catalytic performance of these as-prepared samples was first investigated by cyclic voltammetry (CV) (Fig. 4). From Fig. 4a, PGHS-S-900 shows a *quasi*-rectangular voltammogram without obvious redox peak when the electrolyte was saturated with N_2. In contrast, when O_2 was introduced, a well-defined characteristic ORR peak, centered at -0.262 V with a reaction current of 354 μA after correcting background current, was observed. On the contrary, the peak potential of the ORR for PGHS electrode without doped sulfur atoms shifted slight negatively to -0.27 V and its oxygen-reduction current was measured to be 92 μA (Fig. 4b). Although the result of ICP measurement discovers that S-PGHS-900 contains trace amount of Fe, Mn (Table S3) which may enhance the catalytic activity on the ORR[44], the performance results from the comparison of S-PGHS-900 and PGHS-900 being prepared from the same GO precursor with S-PGHS-900 indicate that the sulfur-doping plays the main positive role on improving the catalytic activity rather than trace metal impurities.[45] Since the charge polarization stemming from the difference in electronegativity between carbon (χ = 2.55) and sulfur (χ = 2.58) is almost negligible, the "electron spin density" may be the dominant factor to regulate the observed ORR activity in the S-PGHS.[46, 47] Compared to S-PGHS-900, S-2DG-900 shows lower ORR catalytic activity with the more negative peak potential (-2.90V) of the ORR and small oxygen-reduction current of 89 μA (Fig. S5a). This can be explained by the fact that PGHS 3D framework facilitates S atoms doping (Table S2, entries 1 and 3) to provide more catalytic activity site for ORR and ensures efficient electron transport and electrolyte ions migration. The influences of the different amount of sulfur source (S-PGHS-900-1-1, S-PGHS-900, S-PGHS-900-5-1) on catalytic activity of ORR were also investigated by CV. As can be seen from Fig. S5b, 4a and S5c, with further increasing the amount of sulfur source (DBDS), the reaction current of the composites (S-PGHS-900-5-1) decreased. The result seems to be depended on the levels of sulfur atoms (Table S2). From Fig. S5d-5f, the catalytic activity of ORR can be also affected by the annealing temperature. With the temperature increasing from 600, 750, 900 to 1000 ^oC, the reaction currents are also improved gradually. This change trend is also observed on the previous reported.[22]

To gain addition insight into ORRs with these as-prepared samples, linear sweep voltammetry (LSV) measurements were carried out on a rotating disk electrode (RDE) for all the PGHS samples as well as a commercial Pt/C electrocatalyst (Fig. 5). Remarkably, S-PGHS-900 displayed a very high ORR onset potential of -0.10 V, being much more positive than that of PGHS-900, S-2DG-900 (Fig. 5a). On the other hand, the ORR reaction current of S-PGHS-900 is also explicitly higher than that of PGHS-900 and S-2DG-900 over the whole potential range. The more positive onset potential as well as the higher reaction current on S-PGHS-900 implies that this material would have clearly better catalytic performance and also verify synergistic effect caused by S-doping and 3D hollow nanospheres framework structure. Increasing the amount of sulfur source, S-PGHS-900-5-1 exhibit a slight negative onset potential than that of S-PGHS-900, agreeing with that of the CV. As a control experiment, the influence of the annealing temperature on the electrocatalytic properties of PGHS was further investigated. Fig. 5b shows the

LSV measurement curves for S-PGHS obtained at 600-1000 °C, and the carbon material obtained at 1000 °C (S-PGHS-1000) displays the highest peak current of all the samples and much positive onset potential, strongly indicating that S-PGHS-1000 has the best ORR activity amongst these carbon materials. It is believed that the enhancement of graphitic degree resulted by restoring defects at higher temperature in the S-PGHS-1000 sample may be one of the factors contributing to the significantly enhanced catalytic activity besides the other factor on the content of sulfur atoms. It is noticeable that the onset potential and reaction current of S-PGHS-900 and S-PGHS-1000 are close to the commercial Pt/C electrocatalyst.

To qualify the ORR process on this novel catalyst, rotating-disk electrode (RDE) measurements on the S-PGHS-900 was performed at various rotating speeds (Fig. 6a). The diffusion current densities are dependent on the rotating rates, and the number of electron transfers (n) and the kinetic-limiting current density (J_k) involved in the ORR can be calculated from the Koutecky-Levich plots (J^{-1} vs, $\omega^{-1/2}$). The plots of S-PGHS-900 at different potentials show good linearity (Fig S6). The electron-transfer numbers (n) of S-PGHS-900 were calculated to be 3.80 at -0.40 V, 3.88 at -0.5V, 3.90 at -0.6V respectively (**equation 1** and **2**), which indicates a four-electron-transfer reaction to reduce oxygen directly to OH^- (Fig. 6b). The calculated J_k value is 12.03 mA cm^{-2} at -0.40 V. These results further confirm that S-PGHS-900 is a promising metal-free electrocatalyst with high catalytic activity for ORRs.

Resistance to crossover effects and stability of the catalyst materials are important requirement for their practical application to fuel cells. The tolerance of S-PGHS-900 to methanol crossover was assessed by the chronoamperometry in comparison with that of the commercial Pt/C catalyst (Fig. 7a). When methanol was introduced into the testing cell, no noticeable change was observed in the ORR current at the S-PGHS-900 electrode, implying its excellent catalytic selectivity for ORR against methanol oxidation. In contrast, Pt/C showed an instantaneous current jump upon addition of methanol. The durability of S-PGHS-900 and Pt/C was also compared (Fig. 7b). From Fig. 7b, after 2000 s testing, S-PGHS-900 displays only a very slight performance attenuation of 4%. In contrast, the Pt/C electrode exhibited a gradual decrease, with a current loss of approximately 18 % under the same periods. The higher catalytic selectivity against methanol oxidation and stability of S-PGHS-900 indicate its great potential candidate for being used in direct methanol and alkaline fuel cells.

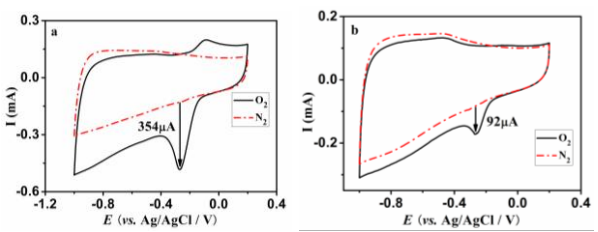

Fig. 4 CVs for the ORR of S-PGHS-900 (a) and PGHS-900 (b).

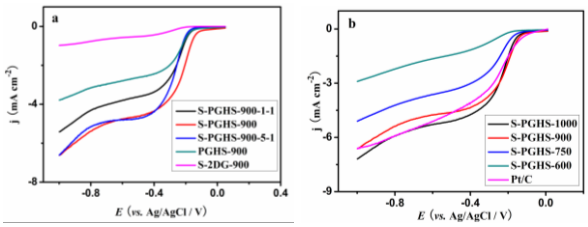

Fig. 5 LSV curves for various PGHS samples (a) and Pt/C catalyst (b) on a glass carbon rotating disk electrode saturated in O_2 at a rotation rate of 1600 rpm.

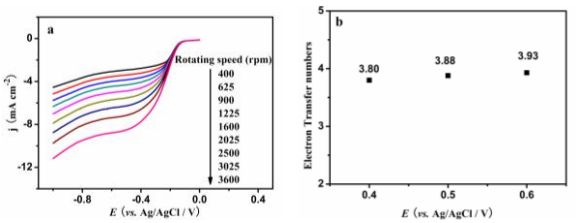

Fig. 6 (a) Rotating-disk voltammograms recorded for the S-PGHS-900 electrode at a different rotation rates. (b) Electron-transfer numbers as a function of the over-potential of S-PGHS-900 at different potential.

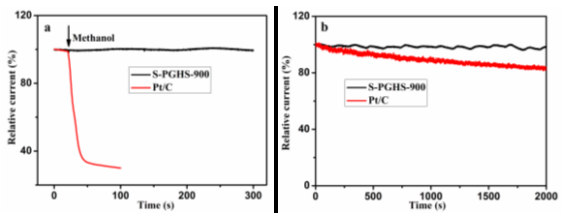

Fig. 7 Chronoamperometric responses of S-PGHS-900 and Pt/C-modified GC electrodes (a) with 3M methanol added at around 20 s and (b) at -0.30 V in an O_2-saturated 0.1 M KOH solution.

To further explore their application potential, the performance of the as-synthesized samples as electrochemical supercapacitors electrode materials was evaluated by CV and galvanostatic charge-discharge measurements. Fig. 8a compares the CV curve of S-PGHS-900 with PGHS-900 and S-2DG-900 at the scan rate of 5 mV s^{-1}. Since the specific capacitance is proportional to the integrated area under CV curve, S-PGHS-900 exhibits a much higher capacitive response than PGHS-900, which indicates that sulfur doped enhances the electrochemical activity of graphene materials. Compared to S-PGHS-900, S-2DG-900 shows the lowest specific capacitance. CVs of S-PGHS-900, PGHS-900, and S-2DG-900 are measured at different scan rate as shown in Fig. 8b and Fig. S7. All the CV curves of the S-PGHS-900 present a rectangular-like shape, and the shape of the curves maintains a slightly distortion even at a scan rate as high as 500 mV s^{-1}, which indicates the highly capacitive nature and the small equivalent series resistance with rapid charging-discharging characteristic. From the correlation of the specific capacitances calculated from the CV curves with the scan rates (Fig. 8c), the average specific capacitance of S-PGHS-900 was calculated to be ~236 F g^{-1} at a scan rate of 2 mV s^{-1} and ~120 F g^{-1} at a high scan rate of 500 mV s^{-1}, ~50.8% of that at 2 mV s^{-1}, suggesting its good rate capability. Whereas the capacitance of PGHS-900 and S-2DG-900 was calculated to be ~64.2 and ~22.6 F g^{-1} at a scan rate of 500 mV s^{-1}, respectively. These results imply that the

capacitive performance of our S-PGHS-900 electrode was synergistically enhanced by the S-doped and 3D hollow nanosphere framework structure.

Galvanostatic charge-discharge measurements were also conducted to highlight the capacitance characteristic of the composites based on PGHS. Fig. 8d shows the plots of voltage versus time of S-PGHS-900, PGHS-900 and S-2DG-900 at current density of 5A g^{-1}. S-PGHS-900 exhibits the longest discharge time, suggesting the highest specific capacitance. The variation of the specific capacitance agrees with the trend of that calculated from CV curves. The plots of voltage versus time of S-PGHS-900 at different current densities (Fig. 8e) and the corresponding specific capacitance calculated are presented in Fig. S8. From Fig. 8e, the charge/discharge curves exhibit almost symmetrical triangle and have not obvious voltage drop (iR) related to the internal resistance during the changing of polarity, revealing its perfect capacitive behavior. Noticeably, S-PGHS-900 shows nonlinear charge-discharge curves and much longer discharging durations at low current densities (0.5 and 0.2 A g^{-1}), due to the presence of some Faradaic capacitances. This may be attributed to oxygen reduction reaction, agreeing with the existence of reductive peak at about 1.7 V in CV curve (Fig. 8a). The calculated specific capacitances are 343 F g^{-1} at 0.2 A g^{-1}, 240 F g^{-1} at 0.5 A g^{-1}, 211 F g^{-1} at 1 A g^{-1}, 191 F g^{-1} at 2 A g^{-1}, 175 F g^{-1} at 5 A g^{-1} and 167 F g^{-1} at 10 A g^{-1}, respectively (Fig. S5). About 70% of specific capacitance is retained when the charge/discharge rate changes from 0.5 A g^{-1} to 10 A g^{-1}. Obviously, these porous RGO hollow nanospheres for supercapacitor materials exhibit excellent rate capability, being consistent with the CV results. This further also confirms that such 3D structure with S-doping is helpful for ion diffusion and charge transfer with high speed at high current density.

Remarkably, the composite S-PGHS-900 electrode demonstrates ~100% coulombic efficiency for each cycle of charge and discharge process and a slight decrease in capacitance (~4%) over 1,000 charge and discharge cycles at a high current density of 5 A g^{-1} (Fig. 8h), which suggesting its high reversibility and excellent electrochemical stability. The impressive electrochemical performance makes it an attractive electrode material for energy storage devices.

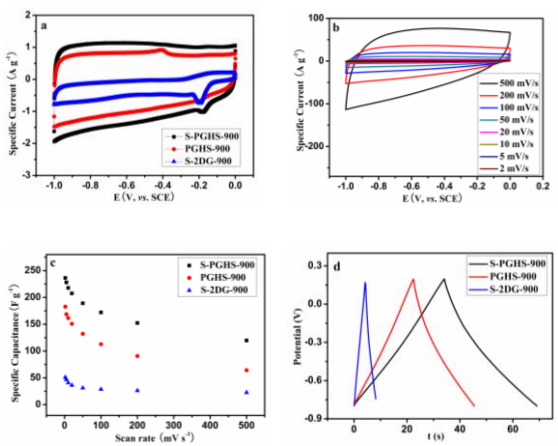

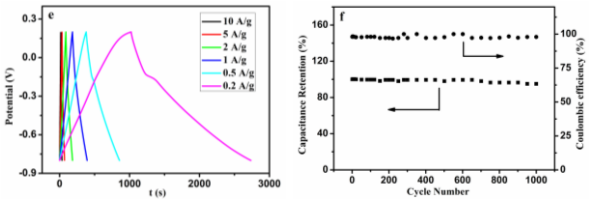

Fig. 8 (a) CV curves of S-PGHS-900, PGHS-900 and S-2DG-900 at a scan rate of 2 mV s^{-1}. (b) CV curves of S-PGHS-900 at different scan rates. (c) Specific capacitance of S-PGHS-900, PGHS-900 and S-2DG-900 as a function of the scan rate. (d) Galvanostatic charge-discharge curves of S-PGHS-900, PGHS-900 and S-2DG-900 at a current density of 5 A g^{-1}. (e) Galvanostatic charge-discharge curves of S-PGHS-900. (f) Cycling stability and coulombic efficiency of S-PGHS-900 at a current density of 5 A g^{-1}.

Conclusions

We have demonstrated the rational design and fabrication of sulfur-doped 3D porous RGO hollow nanospheres framework and investigated its performance both for ORR and supercapacitors in detail. This material exhibits high electrocatalytic activity with four electron transfer for ORR in alkaline medium, and much better methanol tolerance and durability than commercial Pt/C electrodes. Furthermore, this material displays a high specific capacitance, good rate capability and excellent cycling stability as supercapacitor. These good performances are believed to be due to sulfur-doping enhancing electrochemical activity and the 3D porous network structure providing rapid pathways for ionic diffusion and electronic transfer. More importantly, this material with such structure used as conductive matrix may have promising applications in high-performance lithium ion batteries, lithium-sulfur batteries, supercapacitors, chemical sensors and catalysis.

Acknowledgements

The work was supported in part by grants from NSFZJ (LY13E020007), NSFC (51402217, 51420105002, 51272073), NSFC for Distinguished Young Scholars (51025207), Zhejiang Science and Technology Project (2014C31155), and SRFZJED (Y201224027).

Notes and references

[a] *College of Materials Science and Engineering, Hunan University, Hunan Province Key Laboratory for Spray Deposition Technology and Application, Changsha 410082, P. R. China. E-mail: hudacxh@qq.com.*
[b] *Zhejiang Key Laboratory of Carbon Materials, College of Chemistry and materials engineering, Wenzhou University, Wenzhou 325027, P. R. China. E-mail: smhuang@wzu.edu.cn.*
[c] *ARC Centre of Excellence for Functional Nanomaterials, Institute for Frontier Materials, Deakin University, Waurn Ponds, Victoria 3216, Australia.*
† Electronic Supplementary Information (ESI) available. See DOI: 10.1039/b000000x/

1 B. C. H. Steele and A. Heinzel, *Nature*, 2001, **414**, 345-352.
2 E. M. Erickson, M. S. Thorum, R. Vasic, N. S. Marinkovic, A. I. Frenkel, A. A. Gewirth and R. G. Nuzzo, *J. Am. Chem. Soc.*, 2012, **134**, 197-200.
3 A. Goux, T. Pauport and D. Lincot, *Electrochim. Acta*, 2006, **51**,

3168-3172.
4 Z. Y. Lin, G. H. Waller, Y. Liu, M. L. Liu and C. P. Wong, *Carbon*, 2013, **53**, 130-136.
5 N. M. Marković, T. J. Schmidt, V. Stamenkovic and P. N. Ross, *Fuel Cells*, 2001, **1**, 105-116.
6 B. Lim, M. J. P. Jiang, E. C. Cho, J. Tao, X. M. Lu, Y. M. Zhu and Y. N. Xia, *Science*, 2009, **324**, 1302-1305.
7 S. J. Guo and S. H. Sun, *J. Am. Chem.Soc.*, 2012, **134**, 2492-2495
8 C. Z. Zhu and S. J. Dong, *Nanoscale*, 2013, **5**, 1753-1767.
9 Z. Yang, H. G. Nie, X. A. Chen, X. H. Chen and S. M. Huang, *J. Power Sources*, 2013, **236**, 238-249.
10 K. P. Gong, F. Du, Z. H. Xia, M. Durstock and L. M. Dai, *Science*, 2009, **323**, 760-764.
11 Y. Q. Sun, C. Li and G. Q. Shi, *J. Mater. Chem.*, 2012, **22**, 12810-12816.
12 S. Chen, J. Y. Bi, Y. Zhao, L. J. Yang, C. Zhang, Y. W. Ma, Q. Wu, X. Z. Wang and Z. Hu, *Adv. Mater.*, 2012, **24**, 5593-5597.
13 D. S. Yu, K. L. Goh, L. Wei, H. Wang, Q. Zhang, W. C. Jiang, R. M. Si and Y. Chen, *J. Mater. Chem. A*, 2013, **1**, 11061-11069.
14 Y. Zheng, Y. Jiao, J. Chen, J. Liu, J. Liang, A. J. Du, W. M. Zhang, Z. H. Zhu, S. C. Smith, M. Jaroniec, G. Q. Lu and S. Z. Qiao, *J. Am. Chem. Soc.*, 2011, **133**, 20116-20119.
15 J. X. Zhu, D. Yang, Z. Y. Yin, Q. Y. Yan and H. Zhang, *Small*, 2014. 10, 3480-3498.
16 Z. C. Zuo, Z. Q. Jiang and A. Manthiram, *J. Mater. Chem. A*, 2013, **1**, 13476-13484.
17 Q. Q. Li, S. Zhang, L. M. Dai and L. S. Li, *J. Am. Chem. Soc.*, 2012, **134**, 18932-18935.
18 L. F. Wu, H. B. Feng, M. J. Liu, K. X Zhang and J. H. Li, *Nanoscale*, 2013, **5**, 10839-10843.
19 H. J. Choi, S. M. Jung, J. M. Seo, D. W. Chang, L. M. Dai and J. B. Baek, *Nano Energy*, 2012, **1**, 534-551.
20 S. Y. Wang, L. P. Zhang, Z. H. Xia, A. Roy, D. W. Chang, J. B. Baek and L. M. Dai, *Angew. Chem. Int. Ed.*, 2012, **51**, 4209-4212.
21 X. M. Zhou, Z. M. Tian, J. Li, H. Ruan, Y. Y. Ma, Z. Yang and Y. Q. Qu, *Nanoscale*, 2014, **6**, 2603-2607.
22 Z. Yang, Z. Yao, G. Y. Fang, G. F. Li, H. G. Nie, X. M. Zhou, X. A. Chen and S. M. Huang, *ACS Nano*, 2012, **6**, 205-211.
23 D. R. Rolison, J. W. Long, J. C. Lytle, A. E. Fischer, C. P. Rhodes, T. M. McEvoy, M. E. Bourg and A. M. Lubers, *Chem. Soc. Rev.*, 2009, **38**, 226-252.
24 Y. G. Li, W. Zhou, H. L. Wang, L. M. Xie, Y. Y. Liang, F. Wei, J. C. Idrobo, S. J. Pennycook and H. J. Dai, *Nat. Nanotechnology*, 2012, **7**, 394-400.
25 W. Wei, S. B. Yang, H. X. Zhou, I. Lieberwirth, X. L. Feng and K. Müllen, *Adv. Mater.*, 2013, **25**, 2909-2914.
26 X. A. Chen, X. H. Chen, F. Q. Zhang, Z. Yang and S. M. Huang, *J. Power Sources*, 2013, **243**, 555-561.
27 Z. P. Jin, H. G. Nie, Z. Yang, J. Zhang, Z. Liu, X. J. Xu and S. M. Huang, *Nanoscale*, 2012, **4**, 6455-6460.
28 Z. Liu, H. G. Nie, Z. Yang, J. Zhang, Z. P. Jin, Y. Q. Lu, Z. B. Xiao and S. M. Huang, *Nanoscale*, 2013, **5**, 3283-3288.
29 Y. G. Wang and Y. Y. Xia, *Adv. Mater.*, 2013, **25**, 5336-5342.
30 G. Wang, L. Zhang and J. Zhang, *Chem. Soc. Rev.*, 2012, **41**,797-828.
31 H. Jiang, P. S. Lee and C. Z. Li, *Energy Environ. Sci.*, 2013, **6**, 41-53.
32 Li Li Zhang and X. S. Zhao, *Chem. Soc. Rev.*, 2009, **38**, 2520-2531.
33 Y. Wang, Z. Q. Shi, Y. Huang, Y. F. Ma, C. Y. Wang, M. M. Chen and Y. S. Chen, *J. Phys. Chem. C*, 2009, **113**, 13103-13107.
34 X. H. An, T. Simmons, R. Shah, C. Wolfe, K. M. Lewis, M. Washington, S. K. Nayak, S. Talapatra and S. Kar, *Nano Lett.*, 2010, **10**, 4295-4301.
35 M. D. Stoller, S. Park, Y. W. Zhu, J. An and R. S. Ruoff, *Nano Lett.*, 2008, **8**, 3498-3502.
36 L. L. Zhang, R. Zhou, X. S. Zhao, *J. Mater. Chem.*, 2010, **20**, 5983-5992.
37 B. Zhao, P. Liu, Y. Jiang, D. Y. Pan, H. H. Tao, J. S. Song, T. Fang and W. W. Xu, *J. Power Sources*, 2012, **198**, 423-427.
38 L. Dong, Z. X. Chen, D. Yang and H. B. Lu, *RSC Adv.*, 2013, **3**, 21183-21191.
39 L. F. Lai, H. P. Yang, L. Wang, B. K. Teh, J. Q. Zhong, H. Chou, L. W. Chen, W. Chen, Z. X. Shen, R. S. Ruoff and J. Y. Li, *ACS Nano*, 2012, **6**, 5941-5951.
40 Z. Wu, A. Winter, L. Chen, Y. Sun, A. Turchanin, X. Feng and K. Müllen, *Adv. Mater.*, 2012, **24**, 5130-5135.
41 Y. H. Lu, F. Zhang, T. F. Zhang, K. Leng, L. Zhang, X.Yang, Y. F. Ma, Y. Huang, M. J. Zhang and Y. S. Chen, *Carbon*, 2013, **63**, 508-516.
42 N. Xiao, D. Lau, W. H. Shi, J. X. Zhu, X. C. Dong, H. H. Hng and Q. Y. Yan, *Carbon*, 2013, **57**, 184-190.
43 H. T. Liu, Y. Q. Liu and D. B. Zhu, *J. Mater. Chem.*, 2011, **21**, 3335-3345.
44 L. Wang, A. Ambrosi and M. Pumera, *Angew. Chem. Int. Ed.*, 2013, **52**, 13818-13821.
45 Y. Jiao, Y. Zheng, M. Jaroniec and S. Z. Qiao, *J. Am. Chem. Soc.*, 2014, **136**, 4394-4403.
46 I. Y. Jeon, S. Zhang, L. P. Zhang, H. J. Choi, J. M. Seo, Z. H. Xia, L. M. Dai and J. B. Baek, *Adv. Mater.*, 2013, **25**, 6138-6145.
47 W. Kicińskia, M. Szala and M. Bystrzejewski, *Carbon*, 2014, **68**, 1-32.